Repassivation Behavior of Individual Grain Facets on Dilute Ni–Cr and Ni–Cr–Mo Alloys in Acidified Chloride Solution

Kateryna Gusieva,[†,‡] Katie Lutton Cwalina,[†,‡] William H. Blades,[‡] Gopalakrishnan Ramalingam,[‡] John H. Perepezko,[§] Petra Reinke,*,[‡] and John R. Scully[†,‡]

[†]Center for Electrochemical Science and Engineering, and [‡]Department of Materials Science and Engineering, University of Virginia, Charlottesville, Virginia 22904, United States

[§]Department of Materials Science and Engineering, University of Wisconsin—Madison, Madison, Wisconsin 53706, United States

ABSTRACT: The effects of crystal orientation and prior etching on the polarization and repassivation behavior of Ni–Cr and Ni–Cr–Mo alloys have been investigated in acidic chloride environment using dc potentiostatic and ac single-frequency electrochemical impedance spectroscopy. Tests were conducted within the passive region at potentials where local oxide breakdown was possible. Surface morphologies of grains across a wide range of orientations were measured before and after passivation using atomic force microscopy. Oxide growth was monitored on isolated low- and high-index crystallographic planes as a function of repassivation time, enabling the independent measurement of the oxidation and total anodic current densities. Grains exhibited the tendency to either passivate with significant or minimal oxidation or instead resist active passivation and repassivation. The oxidation performance was a function of the crystallographic orientation of the exposed grain surface. The oxides grown on various-orientated surfaces differed in their film growth kinetics, morphology, and steady state thicknesses, even given similar total anodic current densities due to dissimilar oxidation efficiencies. For Ni-11 wt % Cr, only orientations close to (1 0 1) were able to form stable passive films, aided by nanofaceted surfaces with a matchstick-type morphology. On the other hand, all orientations of the Ni-11 wt % Cr-6 wt % Mo alloys formed electrochemically stable oxides films owing to the beneficial influence of Mo on repassivation. Passivation, breakdown behavior, and oxide properties vary with crystal orientation, and this work provides insight into the effects of crystallographic orientation and oxide film morphology on the passivation mechanism of Ni–Cr and Ni–Cr–Mo alloys.
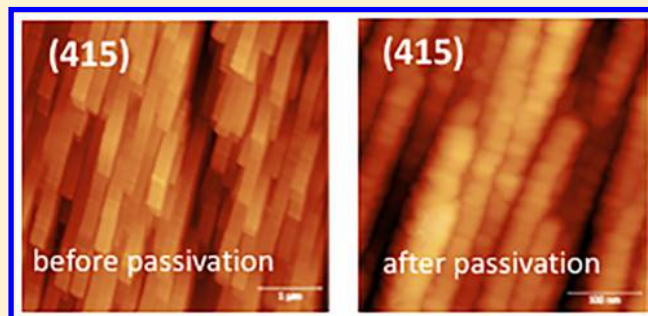
INTRODUCTION

The aqueous and gaseous oxidation rates of alloys frequently depend on crystallographic orientation,[1–20] but a comprehensive understanding of the reaction pathways is rarely established owing to significant experimental challenges, especially when considering orientations far away from low-index surfaces. More attention has historically been paid to the impact of crystallographic orientation on gaseous oxidation,[9–11] motivated by the relevance of oxide surfaces as catalyst supports. Despite the strong experimental evidence that corrosion and passivation are influenced by crystallographic orientation, the number of reports on orientationally resolved aqueous corrosion experiments remains small. Our work establishes an experimental framework to study aqueous corrosion processes in dilute Ni–Cr and Ni–Cr–Mo alloys as a function of crystallographic orientation. This was achieved by using electron beam scattering diffraction (EBSD) to assign the orientations of many grains, followed by alloy patterning and masking to isolate single grains. The masked surfaces were then subjected to controlled electrochemical corrosion studies in combination with atomic force microscopy (AFM) to assess surface morphologies with high spatial resolution. This approach specifically addresses the

formation and performance of the passive layer and the orientation-dependent initial etching and oxidation reaction rates. The direct comparison between global and grain-resolved behavior for the alloys underscores the necessity to consider the impact of crystallographic orientation to fully understand corrosion performance.

The following section introduces a selection of studies concerned with dry and aqueous corrosion and etching of elemental metals and alloys to illustrate the most salient points of this complex issue. For Cu, an fcc transition metal, the oxidation rate decreases from (1 0 0), which shows the fastest kinetics, to (1 1 1) > (1 1 0) and (3 3 1), whereas (1 1 0) and (3 3 1) are nearly identical.[9,11] Oxidation and corrosion of Fe[1,16,17,21] and Al[2,13,15,18] and their common alloys are also well studied. The orientation dependence of localized oxide breakdown leading to pitting corrosion and overall dissolution rates has been reported.[7,15,17–19,22,23] In general, the atom-packing density of a surface is correlated with its reaction rate. A more

densely packed surface such as (1 1 1) reacts slower in dissolution, as well as oxidation and passivation reactions, compared to a relatively open surface such as (1 0 0). The anisotropy in surface atom density for fcc metal surfaces mirrors the anisotropy in surface energy,[24] with low surface energy planes being the least reactive.[25,26] This description of surface reactivity is subject to many caveats including, but not limited to, surface energy changes in alloys through segregation and adsorbates (e.g., chloride ions),[27] modification of reactant transport by grain boundaries, surface diffusion, and crystallography/epitaxy at the metal−oxide interface.

Ni−Cr and Ni−Cr−Mo are the focus of our study. In Ni solid solution crystals, the family of {1 1 1} surfaces exhibits a more noble corrosion potential (E_{corr}) in a 1 N H_2SO_4 solution compared to {0 0 1} and {1 0 1}, implying reduced passive current densities based on mixed potential theory.[28] E_{corr} is more negative with decreasing atomic packing density, and the passive current density follows a corresponding trend with the lowest value measured for (1 1 1) and the highest for lower atomic density.[29] Potentiodynamic polarization studies demonstrated that the degree of protection provided by the electrochemically grown films is maximized for (1 1 1) and minimized for (1 0 0) Ni monocrystal surfaces. The same order for the crystallographic dependence of protection is reported for dry corrosion (e.g., oxidation).[30] The similarity between gaseous and electrochemical oxidation of Ni is manifested in the same order of the oxidation rates.[31] In addition, oxidation rates are often influenced by the crystallographic relation and strain seen for Ni:NiO (1 1 0) and (1 1 4) orientations forming at the interface with Ni (1 1 0) surfaces, while Ni(1 0 0) interfaces with (1 1 1) and (1 0 0) NiO planes, and Ni(1 1 1) favors a single orientation of NiO(−1 1 1).

The transition from pure Ni to alloys containing Fe, Cr, Mo, or W as minor alloying elements introduces additional complexity due to the interplay between compositionally and structurally distinct oxide phases whose contributions are highly sensitive to the details of oxidation and corrosion conditions. In-operando studies on the (1 0 0) surface of Ni-10Cr (at. %) utilizing environmental transmission electron microscopy (TEM) revealed a surface diffusion-controlled oxidation mechanism and the formation of NiO oxide islands with a cube−cube epitaxy.[32] In the later stages of oxidation, NiO and Cr_2O_3 nanocrystals emerged with orientations (1 0 4) and (2 1 0), respectively, primary cubic $NiCr_2O_4$, and secondary NiO oxides.[33] In contrast, the oxidation of Ni-17Cr-7Fe (wt %) in high-temperature water (325 °C) showed a nearly inverted order of oxide formation, starting with a Cr_2O_3 quasi-hexagonal structure appearing as local corrugations on the terraces and step edges of the electrochemically polished (1 1 1) surface,[30] followed by the formation of $Ni(OH)_2$ and various Fe−hydroxide layers at the surface.

Polycrystalline Alloy 22 (Ni-22Cr-13Mo-3W-3Fe), which was subjected to concentrated 3 M HCl, did not form surface oxides, and the dissolution process was the dominant reaction. The corrosion rate scaled inversely with the average coordination number: (1 1 1) < (1 0 0) < (1 1 0).[34] In milder 1 M HCl solution, the corrosion rate accelerated on (1 1 0) surfaces, making (1 0 0) the slower-corroding surface. This behavior was attributed to the competition between dissolution and oxide growth kinetics in the less acidic solution, and the coordination number of surface atoms alone is insufficient for predicting passivation trends. Dissolution during etching can be quantified by the recession of individual grains, as discussed for polycrystalline FePd and Alloy 22.[22,34,35] The alloy dissolution could in this case be directly correlated with the atomic packing density of low- and high-index planes.[22] Irrational crystal planes on polished surfaces dissolved rapidly to form etched, corrugated structures—essentially the rapidly dissolving high-index planes were "etched out of existence" during this process.

The formation of passivating oxides is characterized by a complex interplay between passivation, dissolution, and repassivation rates which all strongly depend on the alloy composition, grain crystallographic orientation, and pH of the aqueous environment. In addition, nucleation and growth of the passive oxide are impacted by the lattice mismatch at the alloy−oxide interface whose role can be diminished in small-grained oxides, where lattice strain is relieved via grain boundaries and dislocations. The crystallographic orientations of metal and oxide and subsequent mismatch accommodation may control defect creation and annihilation. Hence, mismatch is a governing factor, and coordination numbers are not a sufficient but a more relevant descriptor for dissolution rates on oxide-free surfaces.[36]

The occurrence of low- and high-index planes in a given alloy surface is controlled by the metallurgical processing of the alloy prior to passivation; low-index planes are generally more common in textured, undeformed materials while mechanical alloy processing (e.g., rolling, extrusion, etc.), followed by recrystallization, produces a texture with many irrational orientations which need to be considered to fully capture the impact of grain orientation on passivation.[1,14−16,18,22] Our work extends beyond more commonly studied low-index planes to a variety of irrational planes. The grains in an alloy surface were identified using electron backscatter diffraction (EBSD), and subsequently single-grain facets were electronically isolated by masking the surface with an insulating polymer and then interrogated by microscale electrochemistry. The masking of individual grains excludes electrochemical current contributions from adjacent grains but considerably increases the experimental challenges. This approach offers a complete view of the impact of crystallographic orientation and etch-induced faceting on the electrochemical kinetics of passivating systems and the performance of the respective passive layer.

The kinetics of a passivating system under a high electric field ($\sim 10^6$ V/cm) can be analyzed through application of various high-field, thin film oxide growth models.[37−41] In the present study, the Cabrera−Mott model was used to compute kinetic parameters for varying grain orientations passivated in an acidic corrosive environment.[41] This approach has been utilized in previous literature for analyzing the passivation kinetics of various alloys in solutions which induced minimal dissolution.[23,41−43] A similar analysis was used through independent measurement of oxidation and dissolution kinetics, enabling the Cabrera−Mott approach to remain valid. It should be emphasized that alternative high-field-based oxidation models might be considered but are beyond the scope of the current work.[38−40,44]

■ EXPERIMENTAL PROCEDURE

Two Ni solid solution alloys, Ni-11Cr and Ni-11Cr-6 Mo, wt %, have been investigated in this work. The samples were arc-melted, cold-worked to achieve approximately 12% deformation, and subsequently heat treated at 1100 °C for 96 h to produce relatively large recrystallized grains. Following heat treatment, the alloys were successively ground and micro-polished to 1 μm. Microhardness indents were placed across the sample surface to mark the area for EBSD mapping.

Prior to collecting diffraction patterns, the samples were electroetched in 5 M HCl solution with an applied dc voltage of 5 V for 10−20 s to reveal the grain boundaries and produce etched, corrugated, and faceted surface structures. The estimated overall depth of attack was 1.6 μm. EBSD was then performed on the etched surfaces using an FEI Quanta 650 scanning electron microscope at 20 keV to map the grain orientations in the surface. The raw data from the EBSD analysis were processed using the "h k l" software package to extract the Euler angles for determination of the Miller indices (h k l) for the electrochemically tested grains.[45] Given that the sampling depth of a 20 keV electron beam on Ni is greater than 2 μm, the global orientation of grain facets was obtained, rather than the local nanoscale structure altered by etching and accessed by AFM.

To access the electrochemical behavior of single grains, optical photolithography was employed.[46] A AZ300MIF photoresist was spin-coated on the clean sample surface, baked at 110 °C for 90 s, and then subjected to the maximum intensity light under an optical microscope for 3 min to expose the grain of interest. A generic 300MIF developer was used to dissolve the resist from the grains selectively exposed to light. Samples were then baked at 130 °C for 10 min, followed by further baking under UV light for 15 min. Such steps were necessary to ensure the acidic and corrosive electrolyte used in the study did not damage the integrity of the photoresist. Masked grains exhibited a much-improved crevice corrosion resistance that is typical of bulk samples tightly secured into flat cell openings.

The surface topography of single grains was characterized by AFM with an NT-MDT Solver Pro in tapping mode, using ETALON HA/NC tips with a curvature radius below 10 nm. Image analysis was performed using Gwyddion, an open-source software for SPM data analysis.[47] AFM analysis was performed after electroetching, isolation, and masking of the single grains, and the same grains were studied again following the passivation process described later. Ideally, this enables us to directly correlate electrochemical behavior and surface morphology, albeit the experimental challenges in the measurement of electrochemical behavior are considerable. We were therefore not able to seamlessly match both experimental tasks in all instances but obtained a good sample size which enables us to ascertain trends in the relationship between passive film morphology and grain orientation.

Global Electrochemical Measurements. Global electrochemical behavior of the polycrystalline alloys was assessed with dc potentiodynamic polarization and simultaneous ac SF-EIS (single-frequency electrochemical impedance spectroscopy) during potential scans at a fixed frequency using a Gamry potentiostat. The tests were performed in a conventional three-electrode electrochemical cell. The samples were metallographically prepared to a 1200 grit SiC finish, ultrasonically cleaned in methanol, and rinsed with deionized water. The test electrolyte was N_2-deaerated 0.1 M NaCl, acidified to pH 4 using HCl. Prior to acquiring any electrochemical data, any air-formed oxides were minimized via a potentiostatic hold at −1.3 V_{SCE} for 10 min.[48] The ac experiments were performed during upward potential scans from −1.3 to +0.8 V_{SCE} with a 3 mV step. Upon each step, the passive film impedance was measured at an ac amplitude of 20 mV and at a specific frequency which varied with alloy composition but was chosen to reside in the capacitive region of full EIS spectra.[48] Values of 4 and 2 Hz were utilized for large polycrystalline Ni-11Cr and Ni-11Cr-6Mo samples, respectively. Potentiostatic dc polarization at +0.2 V_{SCE} for

10 000 s on polycrystalline Ni-11Cr, Ni-11Cr-6Mo, Ni-22Cr, Ni-22Cr-6Mo, and Ni-22Cr-6Mo-3W (wt %) alloys illustrated the effect of alloying additions on passivation and localized corrosion at an applied passive potential. Oxide thickness was determined through SF-EIS, as explained in detail below.

Local Electrochemical Measurements. Following the partial removal of air-formed oxides, the potential was stepped to +0.2 V_{SCE}. The changes of impedance during the course of passivation of the facets were monitored with SF-EIS under potentiostatic control at a constant, oxidizing potential of +0.2 V_{SCE} and ac amplitude of 20 mV in a deaerated, vertical, three-electrode electrochemical cell in 0.1 M NaCl electrolyte adjusted to pH 4. The specific frequencies used in SF-EIS tests for small electrodes were 10 and 100 Hz for Ni-11Cr-6Mo and Ni-11Cr, respectively, as full EIS spectra indicated that Z'' is dominated by the capacitive behavior of the passive film at these selected frequencies.[48] The applied potential of +0.2 V_{SCE} is not only in the passive range but is also close to the crevice corrosion potential typically seen in NaCl environments and thus technologically significant. The data from grains found to clearly crevice corrode, not repassivate, and exhibit increasing currents were therefore discarded.

Analysis of Electrochemical Data. Several figures are mentioned in this section, and the respective figures are discussed in detail in the Results section for ease of reading.

The oxide thickness, l_{ox}, was calculated using the imaginary impedance component, Z'', using SF-EIS.[48,49] The constant phase element exponent, α, indicated in the full expression, eq 1, can be set to 1 for a purely capacitive oxide layer, an assumption which is supported by fits to the experimental data which yielded $\alpha = 0.95$ and above. Setting α as 1 leads to the expression for l_{ox} given by eq 2, which is applied to our data analysis and used for a simplified comparison between individual grains. In eq 2, f is the applied frequency, ε_o is the vacuum permittivity, ε is the assumed dielectric constant for oxide films on Ni−Cr-based alloys, 30,[50] and A is the exposed grain area. The additional parameter present in only eq 1, ρ_δ, is the characteristic interfacial boundary resistivity for an alloy and its passive film.[49]

$$l_{ox} = \frac{(2\pi\varepsilon\varepsilon_o f)^\alpha |Z''|}{\rho_\delta^{1-\alpha}\sin\left(\alpha\frac{\pi}{2}\right)[1 + 2.88(1-\alpha)^{2.375}]} \quad (1)$$

$$l_{ox} = 2\pi f\varepsilon\varepsilon_o A |Z''| \quad (2)$$

While the observed oxidized surfaces are highly nonuniform, especially at early times, the demonstrated global SF-EIS measurements were used to approximate the relative passivity differences between the presented alloys and crystallographic orientations. The value of ε was also assumed to be constant as its fluctuations following the creation and annealing of defects during passivation processes are not understood. In other work, the oxide thickness determined from eq 2 has shown excellent agreement with other methods of oxide thickness determinations including 3-D atom probe tomography and XPS signal attenuation.

The current density associated with oxidation was calculated from eq 3, where z is the valency of Cr_2O_3, 6, ρ is the oxide density, 5.2 g/cm^3, F is Faraday's constant, and M is molar mass of Cr_2O_3, 152 g/mol. The justification to use Cr_2O_3 as a simplified model for the oxide on the alloys of study is given elsewhere.[48]
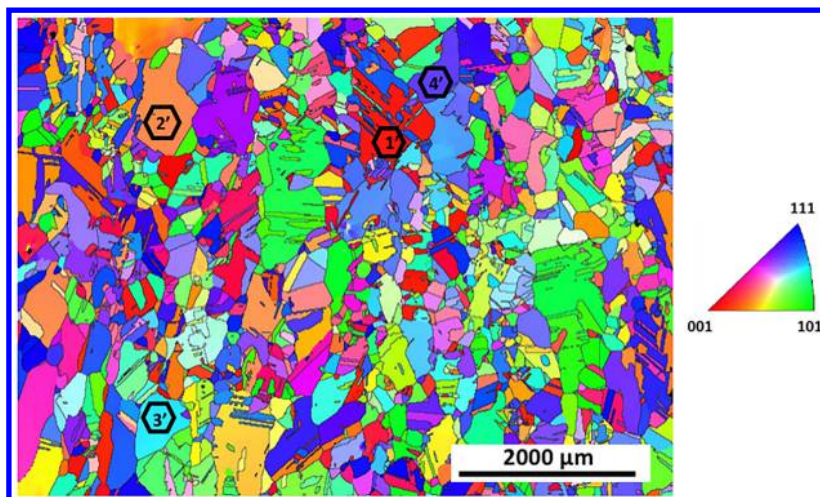
Figure 1. Example crystallographic orientation map obtained using EBSD on Ni-11% Cr-6% Mo with the individual grains chosen for study indicated with hexagons.

$$i_{ox}(t) = \frac{z\rho F}{M}\frac{dl_{ox}}{dt} \tag{3}$$

Through comparison of i_{ox} to i_{total} using eq 4, the overall dissolution during passivation can be obtained:

$$i_{ox} + i_{diss} = i_{tot} \tag{4}$$

The oxide thickness was evaluated using a Pearson product moment correlation coefficient to determine the applicability of inverse logarithmic growth kinetics predicted by the Cabrera−Mott model. (Note: the data were displayed in linear form l_{ox}^{-1} versus log t in order to use the Pearson analysis).[51] Other models such as the point defect and the generalized growth models resulted in poorer fits of $l_{ox}(t)$ once a complete and closed oxide layer was reached.[37,39] The high-field equation (eq 5) and the Cabrera−Mott model solution (eq 6) were applied exclusively to i_{ox}, neglecting i_{total}, to describe the anodic film growth on single crystals and calculate film growth parameters A and B' on individual grains of Ni-11Cr-6Mo.

A and B' are kinetic parameters determined by fitting which contains information about the formation energy of metal cations, electric field, and the energy barrier for diffusion across an oxide.[41]

$$i_{ox} = A \exp\left(\frac{B'V}{q_{ox}}\right) \tag{5}$$

With some rearrangement, eq 5 can be written as:[52]

$$\log i_{ox} = \log A + \frac{(B'V)^{1/2}}{2.3}q_{ox}^{-1/2} \tag{6}$$

The oxide charge density, q_{ox}, was obtained by integrating i_{ox} (Figures 7a and 8a) with A and B' calculated from eqs 7 and 8, respectively, using plots of log i_{ox} vs $q_{ox}^{-1/2}$ where the intercept, b, and the slope, m, were extracted from the linear region of log i_{ox} vs $q_{ox}^{-1/2}$ where $q_{ox}^{-1/2}$ approaches 0 (Figure 8b):[52]

$$A = 10^{-b} \tag{7}$$

$$B' = \frac{5.3m^2M}{zF\rho V} \tag{8}$$

The theoretical A and B', herein referred to as α and β, respectively, were computed using eq 9−11[53−55]

$$i = \alpha \exp(\beta V) \tag{9}$$

$$\alpha = 0.24\frac{qk_BT}{a^2\phi_o\tau}\exp\left(-\frac{\phi_o}{k_BT}\right) \tag{10}$$

$$\beta = \frac{3aq}{8k_BT} \tag{11}$$

where q is the electron charge, k_B is Boltzmann's constant, T is the temperature, 298 K, a is a cation jump distance, assumed as 1.0 nm, ϕ_o is the minimum jump threshold energy (i.e., activation barrier), estimated as 9.7 k_BT_m = 2.26 eV for Cr_2O_3,[55] and τ is the oscillation period, approximated as 10^{-13} s.[53]

The approach to calculate the theoretical film growth parameters was adapted[41] and described via eqs 12−14. Herein, u is the ionic drift velocity, where u_o is assumed as 10^4 cm s^{-1} and z_{mol} is 6 for Cr_2O_3. This approach is used for illustration purposes, and the models mentioned previously may be applied.[41]

$$A_{est} = \frac{zF\rho u}{M} \tag{12}$$

$$u = u_o \exp\left(-\frac{\phi_o}{k_BT}\right) \tag{13}$$

$$B'_{est} = \frac{qaz_{mol}}{k_BT} \tag{14}$$

Analysis of the passivation kinetics using the Cabrera−Mott approach enables more detailed analysis of the effect of grain orientation on the electrochemical growth of passive films in a high electric field.

■ RESULTS

Alloy Grain Size, Texture, and Surface Morphology. The EBSD orientation map, shown in Figure 1, is representative of the deformed and recrystallized microstructure of both Ni-11Cr and Ni-11Cr-6Mo alloys with the presence of a few annealing twins and an average grain diameter of 500 μm. The grains used for electrochemical investigation are indicated by color on the crystallographic orientation map, referenced within a stereographic triangle, and defined by Miller indices and β_i

angles measured from a primary low-index plane, e.g., (0 0 1), (1 0 1), and (1 1 1).[45] Table 1 summarizes the grains orientations used for the electrochemical single-grain analysis and provides their position within the stereographic triangle.

Table 1. Computed ($h\,k\,l$) for the Various Grains Probed Using SF-EIS According to EBSD for Both Ni-11% Cr and Ni-11% Cr-6% Mo, wt %, Where the Orientation Map for the Latter Alloy Is Provided in Figure 1 and the Maximum Measured Oxide Thicknesses, l_{ox}^{max}, Are Reported in Figures 7b and 8a

Grain	h	k	l	l_{ox}^{max}
			Ni-11 Cr	
1	1	1	50	n/a
2	13	1	15	2.4
3	2	1	3	n/a
4	1	0	2	2.4
5	2	1	3	4.6
6	3	1	5	5.5
7	1	0	2	4.4
8	1	0	3	2.9
			Ni-11 Cr-6 Mo	
1'	3	1	26	3.8
2'	3	1	9	1.3
3'	2	1	2	1.2
4'	1	1	2	6.7

Electroetching of the alloys led to dissolution within individual grains, achieving etch depths up to 1.6 μm, and was accompanied by the development of different facet and corrugated morphologies with strong dependence on the orientation of the original polished grains. The SEM (scanning electron microscopy) images shown in Figure 2 illustrate the variation of surface morphology at the micrometer scale. Grains close to (1 0 1) had the greatest overall dissolution depth as well as differences in etch pitting compared to those close to (0 0 1) and (1 1 1). These observations are consistent with the results published by Gray et al.[34] and follow the frequently observed trend that surfaces with low planar atom density are more susceptible to etching.

Qualitatively, (1 0 1) exhibits elongated terraces and steps while (4 1 4), which is 10° away from (1 0 1), can be described by somewhat flatter and narrower terraces. The (0 0 1) surface is considerably rougher, showing no periodicity in any direction, and etching produced "conelike" features. The grains indexed as (2 1 2) are 19° away from (1 1 1), and grains of orientations (4 1 4) and (1 0 1) are still faceting while (0 0 1) shows a rough, but essentially aperiodic, surface morphology. The presence of nanofacets suggests that rapidly corroding grains dissolve and arrive at low-index planes with a lower surface energy and more highly coordinated sites. Therefore, depending on the original polished facet orientation, complicated corrugated structures emerge. It was found that (4 1 4) and (1 0 1) dissolved the most and exposed slower reacting low-index facets, similar to the observations made by Horton et al. during the dissolution of FCC FePd.[22]

Figure 3 includes a selection of surface morphologies imaged with AFM after etching of Ni-11Cr and prior to passivation. AFM affords high spatial resolution and is used here to directly compare pre- and postpassivation morphologies for the same grain (see Figure 10 for postpassivation). Every grain orientation exhibits a characteristic morphology which will consequently impact the corrosion and passivation behavior. The atomic-scale terrace and step structures evolve in a systematic manner within the stereographic triangle. Moving along the edges of the stereographic triangle between the low-index surfaces (e.g., from
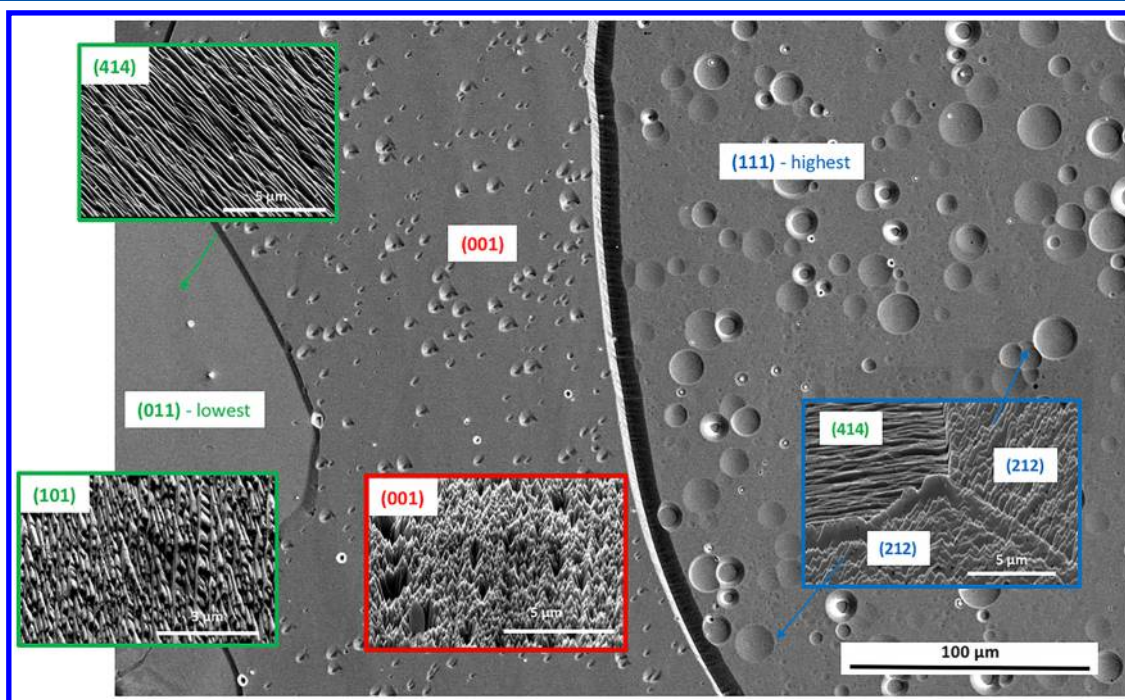
Figure 2. Micrograph of individual grains on Ni-11% Cr, wt %, showing the dissolution, surface corrugation, and faceting following electroetching in 5 M HCl using an applied dc voltage of 5 V for 10−20 s.
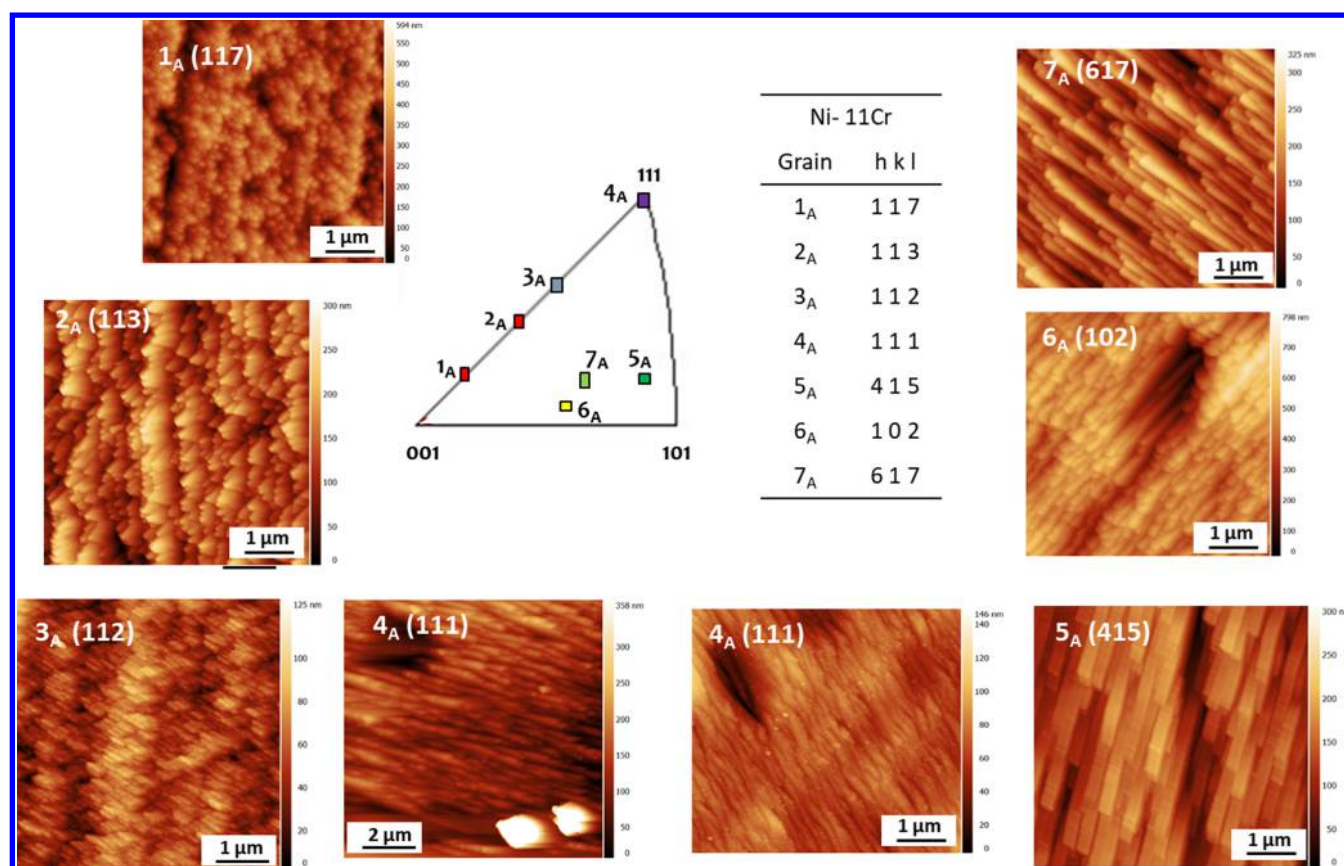
Figure 3. Surface morphologies on various crystallographic orientations of electroetched Ni-11% Cr, wt %, grains as measured using AFM with the corresponding (h k l) indicated in the images, stereographic triangle, and table.
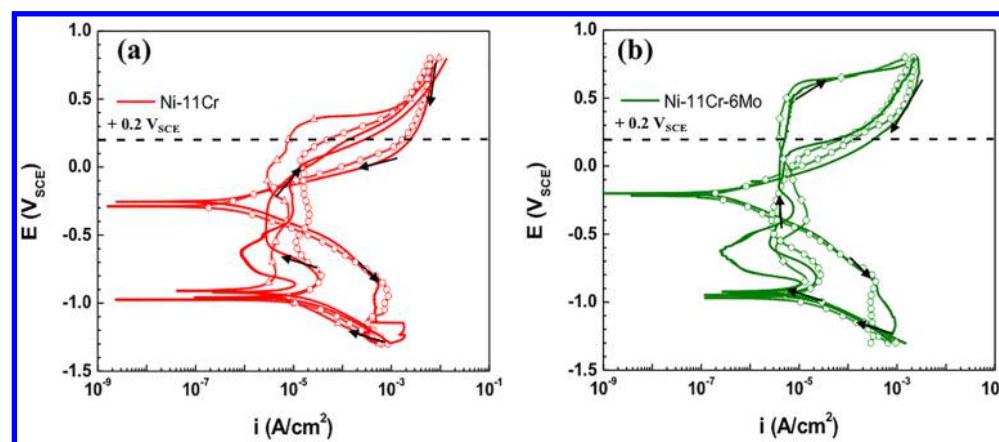
Figure 4. Electrochemical cyclic polarization of (a) Ni-11% Cr and (b) Ni-11% Cr-6% Mo, wt %, in 0.1 M NaCl pH 4 at 1 mV/s with the potentiostatic passivation potential used for the study, +0.2 V_{SCE}, shown schematically to indicate the relative passivation tendencies of the alloys.

(0 0 1) to (1 1 1)) modifies the terrace size and type, while moving away from the perimeter introduces an increasing number of kink sites. Surfaces positioned in the center of the triangle often adopt highly complex surface structures at the atomic scale and are prone to nanofaceting. The combination of complex surface geometries, preferential etching direction, and competition between them defines the overall surface morphologies of the grains studied in this work. The complex surface morphologies significantly impact oxidation and corrosion processes as shown herein.

Grain 1 (Figure 3) in the AFM measurement data set, labeled as G1$_A$(1 1 7), is close to (0 0 1) and shows a very rough, cone-

type, and aperiodic structure which can also be identified in the SEM images of the (0 0 1) surface (Figure 2). Moving toward (1 1 1) on the stereographic triangle, the cones become larger and short wedges develop, as seen for G3$_A$(1 1 2). G4$_A$(1 1 1) is then dominated by wedges with a characteristic wavelike periodicity, which might be described in the framework of morphological instabilities. G5$_A$(4 1 5), which is positioned within the triangle, surprisingly has the largest and best-developed facets arranged in a "matchstick"-type morphology which shows well-developed nanofacets. Images of G7$_A$(6 1 7) and G6$_A$(1 0 2) show a similar matchstick morphology, but the onset of cone formation and transition to structures seen in G3$_A$ and G2$_A$ is already apparent.
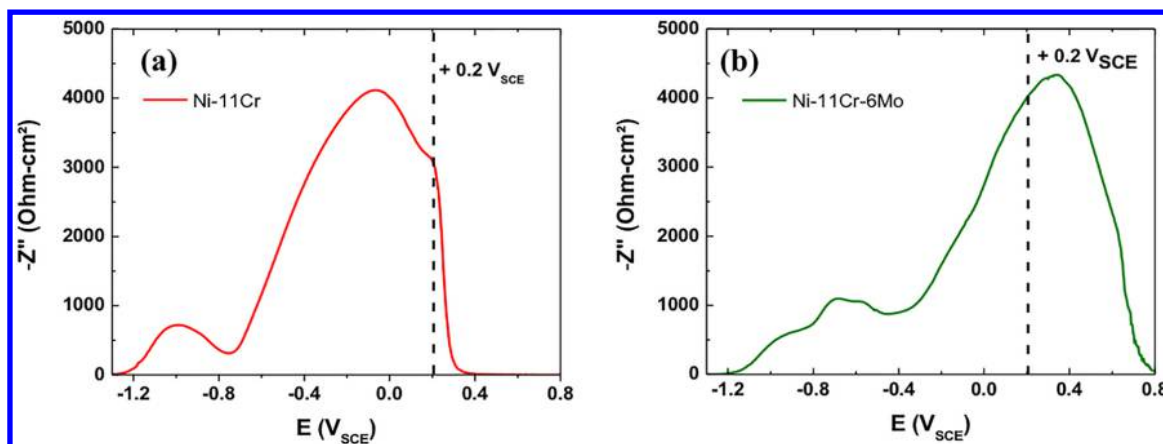
Figure 5. Imaginary impedance ($-Z''$) measurements during the upward potential polarization of (a) Ni-11% Cr and (b) Ni-11% Cr-6% Mo, wt %, in 0.1 M NaCl pH 4 where $-Z''$ corresponds directly to the capacitive behavior of passive films, and thus, l_{ox}, with the potentiostatic passivation potential used for the study, +0.2 V_{SCE}, is shown schematically to indicate the relative passivation tendencies of the alloys.

The surface etching for these samples prior to electrochemical passivation was rather aggressive, and the degree of etching is certainly reduced in less acidic solutions but can be expected to follow the same trends, albeit with less extreme surface height variations. The tendency toward refaceting for surfaces positioned in the center of the stereographic triangle also means that the etch rates (and subsequent passivation rates) of these planes should be included in future, refined models for surface passivation, rather than relying on a description of reaction rates based on average surface atom coordination number for the parent ($h\,k\,l$) orientation.

Global Electrochemical Performance of Polycrystalline Samples. The cyclic polarization data included in Figure 4 show the corrosion kinetics of polycrystalline alloys assessed overall for roughly 50 grains in the deaerated, acidified 0.1 M NaCl electrolyte. The polarization data in Figure 4a indicate a corrosion potential, E_{corr}, of Ni-11Cr alloy between -1.0 and -0.9 V_{SCE}, with the passive region starting from -0.6 V_{SCE}. The pitting potential (E_{pit}) of the alloy was measured around 0 V_{SCE} three out of four times. However, 25% of the time the alloy remained passive at +0.2 V_{SCE}. The measured E_{corr} and E_{pass} of Ni-11Cr-6Mo were similar to those for Ni-11Cr (Figure 5b). However, 50% of the time the E_{pit} of Ni-11Cr-6Mo was above +0.6 V_{SCE}.

The evolution of Z'' (at 10 or 100 Hz) during a upward potential sweep was recorded (Figure 5). As explained for eq 1, Z'' is directly proportional to l_{ox} for a film exhibiting capacitive behavior (i.e., $\alpha \rightarrow 1$).[49] Z'' may increase with l_{ox} or decreasing dielectric constant which is proportional to oxide composition and structure. For both alloy compositions, the plot of Z'' versus E shows two distinct peaks which can be associated with the change in the oxide composition and/or thickness. The magnitude of Z'' was low at the cathodic reduction potentials and started to increase, reaching the first peak at about -1 V_{SCE} for Ni-11Cr and -0.7 V_{SCE} for Ni-11Cr-6Mo. After this initial peak, Z'' decreased, indicating active dissolution within a potential range before the active−passive transition, as seen in the polarization scans in Figure 4. Z'' then sharply increased, signifying passivation of the alloy surfaces with Z'' linearly increasing with E and reaching different maximum values for each alloy before gradually decreasing starting at approximately +0.2 V_{SCE} for Ni-11Cr and +0.4 V_{SCE} for Ni-11Cr-6Mo as seen elsewhere.[56] It is worth noting that at +0.2 V_{SCE}, Z'' was still increasing for Ni-11Cr-6Mo, but the opposite was true for Ni-

11Cr. Such difference in passivity between these two alloys is explained by the well-known effect of Mo synergistically improving passivity when alloyed with Cr especially at high potentials.[48,57−61]

The eventual decrease in Z'' for both alloys occurred over a range of potentials, -0.2 to +0.4 V_{SCE} for Ni-11Cr and +0.4 to +0.8 V_{SCE} for Ni-11Cr-6Mo, indicating the thinning of the oxide and/or transpassivity rather than a sudden, sharp decline, as is the case for pitting or crevice corrosion. Transpassivity, rather than pitting, is well supported on the basis of calculated Nernst potentials at pH 4 for Cr oxidizing from +3 to +6 and Ni from +2 to +3. The potentials are similar for both reactions: +0.55 V_{SCE}.[62] This assumption is further supported by the near zero values of Z'' from +0.4 to +0.8 V_{SCE} for Ni-11Cr (Figure 5a), indicating the oxide is dissolved relatively uniformly in that region. Moreover, some oxygen evolution is possible (+0.78 V_{SCE}), as suggested by return downward scans with small, positive hysteresis and subsequent high open circuit potentials (Figure 4).

Figure 6 shows anodic current transients for several Ni-based alloys during potentiostatic holds at +0.2 V_{SCE}. The total current densities were similar for all the alloys during the first 100 s of oxide growth, except for Ni-22Cr-6Mo-3W, which had a current density that was 1 order of magnitude lower. The passive current
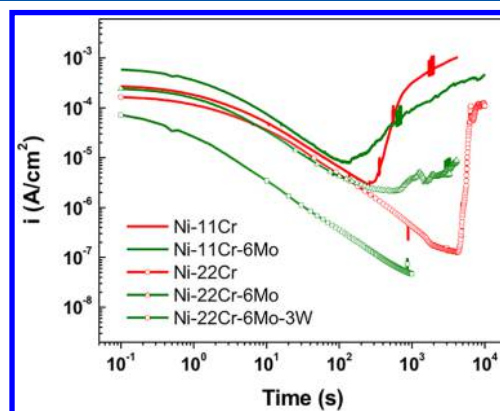
Figure 6. Current decays during the passivation of various Ni−Cr-based alloys at the potential of interest, +0.2 V_{SCE}, for 10 ks, where the current decay indicates film growth and increases correspond to film breakdown and propagation.
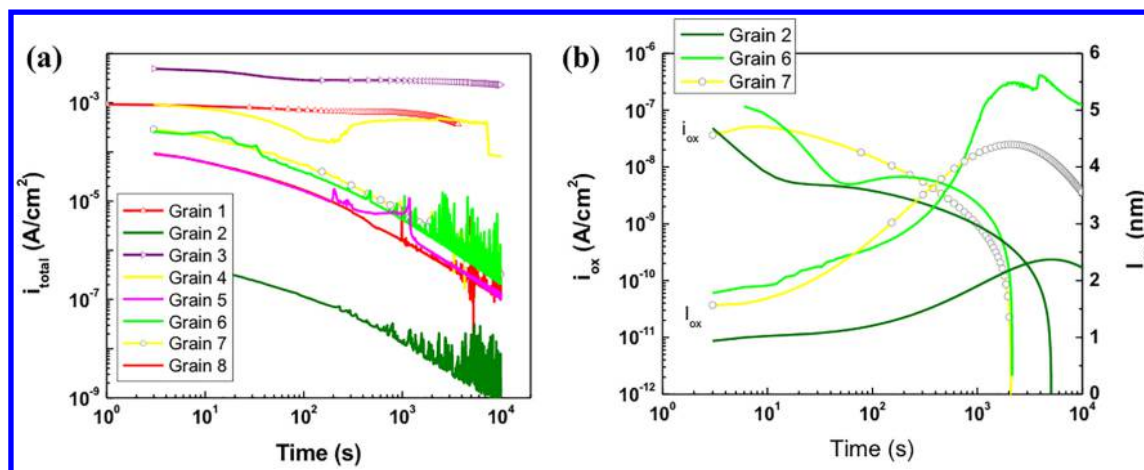
Figure 7. Electrochemical passivation at +0.2 V_{SCE} of various grains of Ni-11% Cr, wt %, as indicated in the stereographic triangle inset in Table 1 in 0.1 M NaCl pH 4 for 10 ks where (a) the overall current decays are shown for every grain and (b) those capable of repassivation were analyzed using SF-EIS in order to extract the oxidation current density (i_{ox}) and thickness evolution (l_{ox}).

density decayed at first, as predicted by high-field growth kinetics (eq 5), and then suddenly increased when crevice corrosion was initiated at different times on each alloy besides Ni-22Cr-6Mo-3W. Crevice and pitting corrosion were observed after step potential passivation on Ni-11Cr-6Mo after 100 s, Ni-11Cr after 270 s, and at longer times or not at all for Ni-22Cr, Ni-22Cr-6Mo, and Ni22Cr-6Mo-3Mo, respectively. These experiments establish that +0.2 V_{SCE} is a potential of significant interest where repassivation and possible breakdown can occur, as seen in Figures 4−6.

Local Electrochemical Performance of Ni-11Cr Single Crystals. The current−time transients shown in Figure 7a describe the anodic oxide growth on individual grains of Ni-11Cr. No crevice corrosion was observed at the edge of any masked grain areas for the tests shown. The position of the grains in relation to the low-index planes is provided in Table 1. During passivation, a decrease in the total anodic current density, i_{tot}, was observed. For most grains on Ni-11Cr, i_{tot} remained high and did not reach a steady state limit during the 10 000 s potentiostatic hold. Any positive current transients indicate local oxide breakdown and pitting events. The failure of most grains to reach a steady state low i_{tot} suggests that the passive films on Ni-11Cr frequently break down and corrode at +0.2 V_{SCE} (Figure 4a). However, the current densities differed from grain to grain, with G2(13 1 15), for instance, possessing a current density several orders of magnitude lower than G5(2 1 3). This demonstrates that in acidic conditions (i.e., an environment which favors significant dissolution), passivation indeed depends on the grain orientation.

Many grains of Ni-11Cr alloy passivated and exhibited metastable breakdown events while others did not (Figure 7a). The low number of passivated grains can be attributed to the dilute bulk Cr level, low pH, high potential, and the absence of Mo or W. Along with those that underwent electrochemical breakdown, G1(1 1 50) and G3(2 1 3) did not passivate. In addition, the statistical distributions associated with corrosion reactions[63−65] and the complex interplay between filming and dissolution-induced undercutting sometimes resulted in similar grain orientations exhibiting vastly different electrochemical passivity despite identical preparation procedures. The passivation tendency of a grain relies on specifying more details than just {h k l} of the grain boundary plane exposed. This is particularly evident for G5(2 1 3) which is a grain with the same

(h k l) as G3(2 1 3) within the error margin of orientation analysis, but G3 showed a very high i_{EC}, which strongly indicated an experimental issue, and these data were not included in the analysis. G4 with the same (h k l) as G7 indicates a highly unusual i_{total} behavior over time as seen in Figure 7. In this case the observed behavior is most likely due to failure of the photoresist during the experiment.

However, the combination of low Cr content of Ni-11%Cr, the acidic environment, the relatively high applied potential, and the (h k l) dependency combined to create a condition where some grains will not passive which by themselves does not imply experimental artifact; these results are real. Passivation should be regarded as interface-controlled and occurs grain by grain. The measured $i_{ox}(t)$ and $l_{ox}(t)$ are shown in Figure 7b for the passive grains where the photoresist did not fail: G2(13 1 15), G6(3 1 5), and G7(1 0 2).

G2(13 1 15) showed a 2 orders of magnitude lower passivation current density compared to G6(3 1 5) and G7(1 0 2). However, i_{ox} was not significantly different. This points to a much higher passivation efficiency in G2(13 1 15) compared to G6(3 1 5) and G7(1 0 2). i_{ox} also drops to very low values between 2000 and 6000 s as the total current maintains the oxide thickness at a quasi-steady state thickness as discussed elsewhere.[48]

All passivating grains exhibited a gradual increase in oxide thickness during the first 1000 s of oxidation but at different rates. The i_{ox} of G6(3 1 5) and G7(1 0 2) were somewhat similar, and oxides were of similar thicknesses at 1000 s. The thickness of the oxides is summarized in Table 1, and no l_{ox} is given for the grains which did not repassivate. The average l_{ox} started to reduce on G7(1 0 2) after 1000 s, due to most likely chemical dissolution but could also be caused by a decrease in ε as the initially defective film self-anneals. This effect, however, has yet to be quantified, and as such we assumed a constant value of ε in our calculations. The film dissolution on G6(3 1 5) and G2(13 1 15) was delayed by approximately 100 and 500 s, respectively, compared to G7(1 0 2). The thickest oxide was formed on G6(3 1 5) (5.0 nm), followed by G7(1 0 2) (3.7 nm), and the thinnest on G2(13 1 15) (2.3 nm). These are in good agreement with the film thicknesses measured on Alloy 22,[56] Ni-22Cr, and Ni-22Cr-6Mo[48] during potentiostatic polarization in 5 and 0.1 M NaCl solutions, respectively. G2(13 1 15) has the thinnest oxide with the highest resistance to dissolution, and thus the lowest total
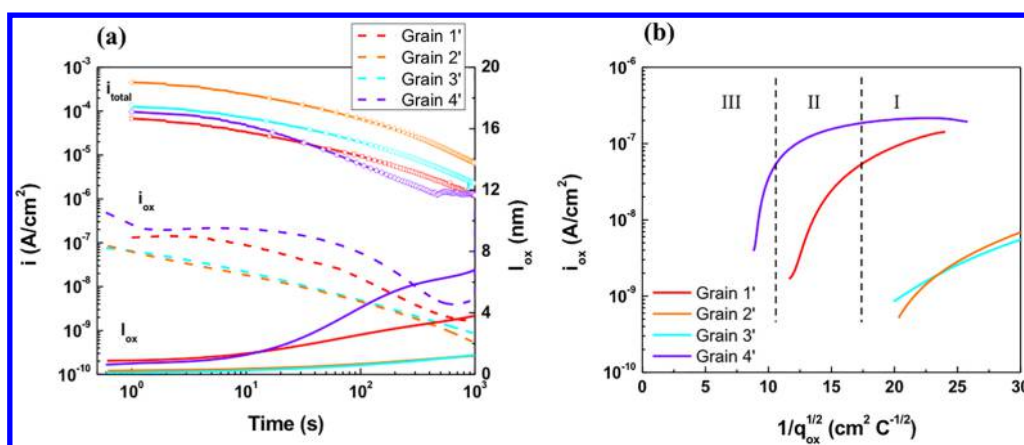
Figure 8. (a) Electrochemical passivation at +0.2 V_{SCE} of various grains on Ni-11% Cr-6% Mo, wt %, as indicated in the stereographic triangle inset in Table 1 in 0.1 M NaCl pH 4 for 10 ks where SF-EIS analysis extracted i_{ox} and l_{ox} for each grain. (b) Passivation kinetics were analyzed for each grain in the linear region as $i_{ox} \rightarrow 0$ according to the Mott−Cabrera model, and the corresponding numerical results are summarized in Table 2.

Table 2. Oxidation Kinetic Parameters Computed for Ni-11% Cr-6% Mo, wt %, During Passivation at +0.2 V_{SCE} for 10 ks in 0.1 M NaCl pH 4 Using the Mott−Cabrera Approach Compared to the Theoretical α, β, A_{est}, and B'_{est} Established by Previous Literature (See Text for Details)[a]

Grain	B', cm/V	A, A/cm^2	β, cm/V	α, A/cm^2	B'_{est}, cm/V	A_{est}, A/cm^2
1′	5.7×10^{-6}	3.2×10^{-14}				
2′	5.4×10^{-6}	2.0×10^{-13}	7.3×10^{-9}	1.0×10^{-28}	1.2×10^{-7}	1.2×10^{-26}
3′	1.9×10^{-6}	3.4×10^{-11}				
4′	3.1×10^{-4}	2.1×10^{-17}				

[a]A and B' correspond to the experimentally-calculated kinetic growth constants during Region III thickening, whereas the pairs of α and β, A_{est}, and B'_{est} are theoretically-derived constants based on the high-field[53−55] and Cabrera−Mott[41] models, respectively.

current density. As such, G2(13 1 15), whose orientation is very close to (1 0 1), develops a highly efficient passive layer (Figure 7a). The i_{total} is significantly larger than i_{ox}, suggesting inefficient passivity of the alloys. Faster oxide growth, exhibited by G6(3 1 5) and G7(1 0 2), may result in the formation of a more defective metastable oxide and, thus, a higher susceptibility to eventual breakdown at increased values of i_{total}. In general, all grains on Ni-11Cr demonstrated a high i_{total} with low oxidation efficiency, even on grains which repassivated. The passivating grains do not have an exact match in the AFM images but lie within the region of "matchstick" morphology defined by G5$_A$ to G7$_A$ (see Figure 3). All other grains are in the regime of aperiodic and wavelike morphologies which do not present well-defined facets.

Local Electrochemical Performance of Ni-11Cr-6Mo Single Crystals. The total and oxide current densities recorded during passivation of Ni-11Cr-6Mo grains are plotted in Figure 8a. As opposed to Ni-11Cr, the current decay occurred without pitting or crevice corrosion almost always due to the beneficial effects of Mo. This points to the assertion that passivity occurs grain by grain and is shifted towards propensity for repassivation with Cr and Mo despite harsh pH, potential, and unfavorable grain orientation. The measured i_{total} was roughly similar for all grains, but it was much greater than extracted i_{ox} indicating, again, the inefficiency of oxidation processes. The i_{ox} and l_{ox} differed by approximately an order of magnitude from grain to grain with i_{ox} decreases G4′(1 1 2), which was slightly larger than G1′(3 1 26) and a magnitude higher than G2′(3 1 9) and G3′(2 1 2). G2′(3 1 9) and G3′(2 1 2) show slight differences in the time dependence of i_{ox}. After 1000 s of electrochemical passivation, oxide growth was proportional to the variations in i_{ox}. The film thickness follows the order of i_{ox}: G4′(1 1 2) (6.8

nm), G1′(3 1 26) (3.8 nm), G2′(3 1 9) (1.3 nm), and G3′(2 1 2) (1.2 nm).

The oxide growth kinetics were analyzed using the data presented in Figure 8b. Three different regions can be distinguished on the plots in Figure 8b. Taking G1′(3 1 26) as an example, Region I can be ascribed to the earlier stages of oxidation where the oxide starts to nucleate into widely spaced islands.[10,32,33,66,67] At this stage passivation is likely controlled by surface diffusion or cation ejection. However, as the oxidation progresses, the oxide islands start to coalesce (Region II) with a concomitant reduction in growth rate. Oxidation is controlled by defect diffusion through the oxide or cation ejection at the metal/film interface during this stage.[10] During the latter Region III, the film may uniformly cover the surface, and thus growth is controlled by transport or interfacial cation injection as assumed in the Cabrera−Mott model. The sloped linear trend in Region III is used for extracting the film growth parameters, A and B' (Table 2), as it corresponds to the thickening of a conformal layer rather than the kinetics of nucleation and growth of individual particles. Figure 9 demonstrates that, in this region, the oxidation growth kinetics correspond well to the inverse logarithmic growth law predicted by the Cabrera−Mott model.[39] As such, the use of the kinetic model is validated for this type of oxide growth.

Impact of Surface Morphology and Faceting on Oxide Growth. The surface morphologies of the electroetched grains of Ni-11Cr after 100 s of oxidation at +0.2 V_{SCE} are displayed in Figure 10a. As such, the AFM images were obtained at the onset of Region III oxide growth, as indicated in Figures 8 and 9, where fully conformal, terminal oxides are not yet fully developed. This enables us to still see surface roughness influenced by original nucleation sites. Oxidation is recognized in the images as an
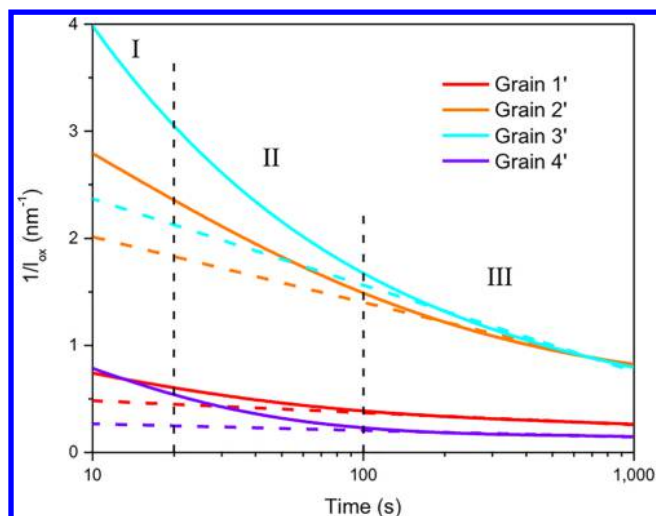
Figure 9. Inverse logarithmic growth trends (dashed line) fitted to the Region III oxidation data previously presented in Figure 8 (solid line), where the apparent good fit indicates the applicability of the Cabrera–Mott model for analysis of the film growth kinetics.

increase in roughness on a facet and/or as discrete oxide nodules which break the periodicity of the surface morphology. On $G4_A(1\,1\,1)$, relatively large oxide nodules about 100 nm in size

are readily apparent and form on the wavelike morphology. At the same time, the wave crests have increased in roughness and are covered with oxide. On the matchstick morphology of the $G5_A(4\,1\,5)$ and $G7_A(6\,1\,7)$ grains, oxide nuclei have merged to form a continuous and quite homogeneous cover. The morphology of the rather rough and aperiodic $G1_A(1\,1\,7)$ surface, on the other hand, does not change during oxidation except for a small variation in the sharpness of the peaks and valleys as seen in line scans. The nucleation of a large number of very small oxide nuclei cannot reduce the overall surface roughness, and the high corrugation remains, likely contributing to oxide breakdown. The morphology of the Ni-11Cr-6Mo surface is similar to that observed on Ni-11Cr, and the grain shown is positioned close to 3′, as defined in Table 1. It presents the wavelike morphology seen for $G1_A$, but with a considerably longer wavelength approaching the transition to the matchstick morphology. Variation in surface morphology is likely not the origin of the different passivation behavior between alloys with and without Mo.

The variation in the surface morphology will impact the progression of the passivation reaction; a large roughness tends to reduce reactant diffusion on the surface and thus increases oxide island density. $G1_A$ presents a rough surface, providing many areas for local breakdown due to sharp structures,
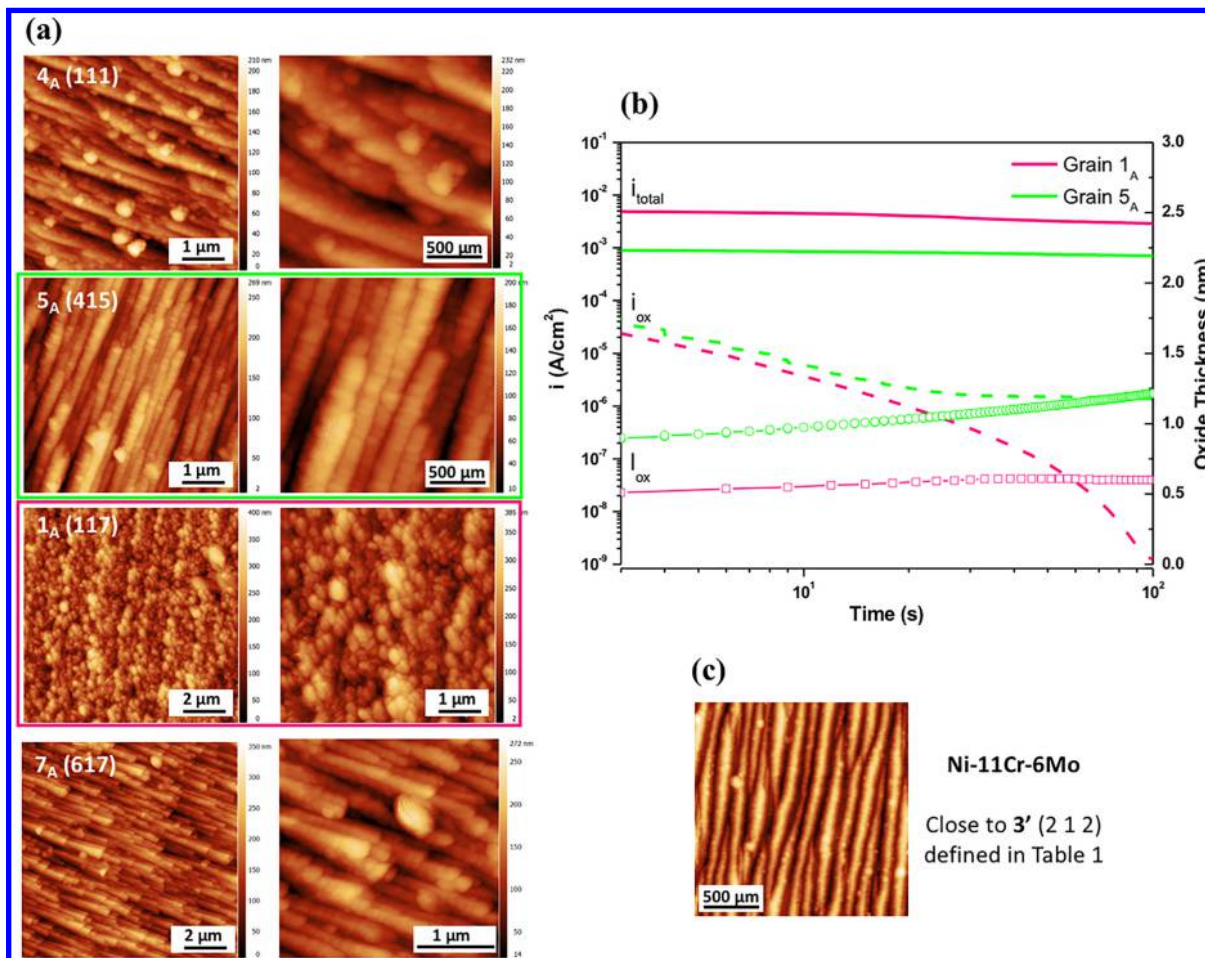
Figure 10. (a) AFM images of individual Ni-11% Cr grains after 100 s of passivation in 0.1 M NaCl pH 4 at +0.2 V_{SCE}. The corresponding images after electroetching and before passivation are shown in Figure 3. (b) The computed i_{total}, i_{ox}, and l_{ox} using SF-EIS analysis of $G1_A(117)$ and $G5_A(415)$. (c) AFM image of a Ni-11Cr-6Mo grain after passivation.

numerous oxide grain boundaries, and incomplete and inhomogeneous oxide coverage.

Figure 10b shows an example of total oxide current versus time recorded during oxidation of $G1_A(1\ 1\ 7)$ and $G5_A(4\ 1\ 5)$, providing a direct comparison of surface morphology after oxidation and the corresponding electrochemical signature. The passive film on $G1_A(1\ 1\ 7)$ is thinner than the oxide layer on $G5_A(4\ 1\ 5)$ and forms quickly without increasing significantly in thickness overall for all times during the experiment as i_{ox} drops toward 0. The overall i_{total} for $G1_A(1\ 1\ 7)$ is higher than that for $G5_A(4\ 1\ 5)$ despite the decreased i_{ox}. This suggests that $G5_A$ is more passive than $G1_A$. In general, the results indicate that grains oriented closer to $(1\ 0\ 1)$ on Ni-11Cr passivate faster and more easily than those between $(0\ 0\ 1)$ and $(1\ 1\ 1)$. Similar behavior is seen in Figure 7, where only the grains with orientations close to $(1\ 0\ 1)$ were able to repassivate at long times. This observation is directly related to the specific surface morphology—rough on a very short length scale, with sharp features for the grains closer to $(0\ 0\ 1)$ possessing poor passivation properties, and with nanofacets expressed in the matchstick morphology for the grains closer to $(1\ 0\ 1)$ exhibiting better passivation. The other grains either did not form a continuous film or broke down fully following localized pit initiation.

■ DISCUSSION

Cabrera and Mott hypothesized that thin film growth was directly dependent on the migration of interstitial cations from the metal/film interface to the film/solution, where the rate-limiting step is cation injection from the metal.[41] The electric field, which is assumed to be uniform, triggers a shift in the Fermi level across the oxide film, also called the Mott potential, and drives ionic transport and electron tunneling. It is inappropriate to determine kinetic growth parameters from i_{total} due to substantial and often dominant dissolution kinetics for both single crystals and polycrystalline surfaces during aqueous passivation, and thus only i_{ox} versus q_{ox} should be used. At longer times ($t > 100\ s$) where the oxide growth is dominated by the thickening of conformal layers after island coalescence, the observed oxidation kinetics agrees well with inverse logarithmic kinetics predicted by the Cabrera−Mott (C−M) model and its aforementioned assumptions (Figure 9). The experimentally obtained values for A and B' kinetic parameters were compared to the theoretical values of α, β, A_{est}, and B'_{est} (Table 2) using i_{ox} in Region III (Figure 8b). The calculated values of A for single grains were significantly higher than the theoretical estimations, e.g., 10^{-11}–10^{-17} versus 10^{-26}–10^{-29} A/cm^2, whereas the experimental B' versus theoretical β and B'_{est} were noticeably closer: approximately 10^{-4}–10^{-6} vs 10^{-7}–10^{-8} cm V^{-1}, respectively.

Theoretically, A and B' quantitatively describe the energetic activation barrier and physical cation jump distance relative to the thermal energy for defect transport, respectively. The similarity of the theoretical and experimental B' values suggests that C−M applies for quantifying the jump distance associated with the activated step in crystals with periodic potentials. The orders of magnitude difference in A suggest, however, that the activation energy barrier is not as easily quantified. This is likely due to the exponential dependence of α and A_{est} on ϕ_o, a parameter which was roughly estimated to be 2.23 eV using the crystal melting temperature. A change in only 1 eV results in many orders of magnitude difference in α and A_{est}. For example, to match the median experimentally determined A (1.1×10^{-13} A/cm^2) to the theoretical values of α and A_{est} (Table 2 and

Figure 8), ϕ_o would only need to be 1.47 eV. This value is likely more accurate for the alloy surfaces presented as it takes into account growth kinetics, unlike the overly simplistic literature estimation based solely on thermodynamic considerations, 2.3 eV, and agrees with a previously reported value for cation diffusion in NiO, 1.6 eV.[53,68]

The present study includes a direct comparison between Ni-11Cr and Ni-11Cr-6Mo which confirms the better passivity across many grains in polarization scans (Figure 4), in Z'' versus potential (Figure 5), and during potentiostatic holds for potential step repassivation in the alloy containing Mo (Figures 8−10). The global performance of Ni-11Cr-6Mo is mirrored in the study of single grains. A fair number of Ni-11Cr grains are incapable of repassivation at long times (Figure 7a), while every grain on Ni-11Cr-6Mo repassivated even for unfavorable irrational crystal orientations and nanoscale surface morphology (Figure 8a). The grain orientations are distributed throughout the stereographic triangle and include regions of good passivation close to $(1\ 0\ 1)$ for Ni-11Cr and regions prone to "failure to passivate" closer to $(0\ 0\ 1)$ for Ni-11Cr. The addition of Mo as a minor alloying element greatly impacts the repassivation and improves the resistance to localized break-down of the oxide layers. The indication is that overall passivation occurs grain by grain under the conditions examined and some grains do not meet the criteria in the Ni-11Cr alloy.

Ni−Cr−Mo alloys are dominated by Cr-rich films when a critical composition of 10−12 wt % Cr exists in solid solution.[69−72] The mechanism as to why Mo is so beneficial to passivation remains less certain.[73] The presence of Mo(VI), Mo(V), and/or Mo(IV) cations in oxides has been observed in stainless steels[60,74−84] and Ni-based alloys,[59,61,85−88] where some Mo-oxides are embedded in the passive layer. The solute vacancy interaction model, an extension of the point defect model, proposes that oxidized Mo is beneficial toward passivity and preventing pitting-type film breakdown because it attracts and captures cation vacancies, thus preventing the formation of detrimental vacancy clusters.[89,90] More recently, DFT work demonstrated that Mo stabilizes the adsorption of O on Ni-22 wt % Cr surfaces, thus facilitating oxidation.[91] From the single-grain experiments, it is evident that alloys with Mo provide much less variability of passivation performance across many crystallographic orientations. This can be due to modification of passive film nucleation and growth or the domination of local oxide defect chemistry attributes, such as the vacancy sequestration described above. Mo alloying evens out the significant differences in passivation performance between grains observed for Ni-11Cr, thus enhancing the quality of the passive layer and unsuing ability to repassivate.

The strong correlation between crystallographic orientation and surface reactivity, which includes etching as well as passivation, is at the core of our work. The Ni-11Cr alloy exhibits a significant variation in etch rate and subsequent passivity with crystallographic orientation. The orientation dependence of etching has often been described within the framework of coordination number (CN), where the surface with the highest average surface CN, and thus highest planar atom density, is least reactive, which is also the result for our alloys.[22] For an fcc lattice, the $(1\ 1\ 1)$ surface has a CN of 9, followed by $(1\ 0\ 0)$ with a CN of 8, and $(1\ 0\ 1)$ with a CN of 7. Moving from the $(1\ 1\ 1)$ surface along the $[1\ -1\ 0]$ and $[0\ 1\ -1]$ zone axes to $(1\ 0\ 1)$ and $(0\ 0\ 1)$, respectively, decreases the CN but also introduces terraces of varying widths and orientation at the atomic scale. All other surfaces which are not positioned on

these zone axes will develop kinked step edges and complex surface structures and reconstructions that are often poorly understood. In parallel to the overall loss of material, the surfaces undergo complex changes in their surface morphology. Electrochemical etching of Ni-11Cr surfaces prior to passivation was particularly aggressive in our experiment, but similar surface reactions and identical morphology evolution are expected in less acidic solutions, albeit with smaller overall recession and less extreme height variations.

The evolution of complex surface morphologies during etching can be attributed to a preferential etching of the lowest CN planes while other planes recede at a slower rate. For example, the pristine $G3_A(1\,1\,2)$ surface has $(1\,1\,1)$ terraces and $(0\,0\,1)$ steps, which is inverted for $G1_A(1\,1\,7)$ which exhibits $(0\,0\,1)$ terraces and $(1\,1\,1)$ steps. $G2_A(1\,1\,3)$ has a $(1\,1\,1)$ terrace that is only one atom wide and is at the transition to the $(0\,0\,1)$ terrace. $G4_A(1\,1\,1)$ is the end point and represents what has been identified as the slowest etching surface.[92,93] We can therefore expect a faster etching of the $(0\,0\,1)$ terraces for $G1_A(1\,1\,7)$, exposing a larger area of the more stable $(1\,1\,1)$ step surface and leading to substantial surface roughening. The AFM images in Figure 3 show high aspect ratio asperities and a rather rough surface for this grain. A highly corrugated morphology is also seen in the SEM images for the $(0\,0\,1)$ surface (Figure 2). For $G3_A(1\,1\,2)$, which has a slower reacting $(1\,1\,1)$ terrace, the surface roughening is reduced. The transition in terms of surface roughness and structure is gradual along the $[0\,1\,-1]$ zone axis.

In the hierarchy of surface morphologies, differential etch rates can lead to energetically unstable surfaces which then undergo faceting on the nano- or mesoscale. Surface relaxation by faceting is seen in the grains $G5_A(1\,1\,7)$, $G6_A(1\,0\,2)$, and $G7_A(6\,1\,7)$, with $G5_A(1\,1\,7)$ showing the most pronounced expression of faceting. All these surfaces are positioned inside the stereographic triangle, and their ideal surfaces would have high-density kink and terrace populations and often correspondingly high surface energies, which are the driving force for faceting during chemical dissolution. Future AFM studies aim to include a larger number of grain orientations and develop additional experimental techniques to unravel the orientation of nanofacets.

Discussion and assessment of the etching process is a first step toward capturing the differential, orientation-dependent reaction rates. In contrast to etching, the passivation process is accompanied by the formation of an oxide which introduces an interface, misfit dislocations as sources and sinks for point defects, and additional energy terms such as lattice strain for crystalline oxides. The orientation-dependent passivation behavior is complex, and the present study establishes an experimental framework to unravel this important aspect in the passivation and breakdown behavior of technical alloys. Our interpretation, so far, is that the favored orientation and nanostructure during passivation may have more to do with orientations favorable for oxide epitaxy compared to surface energy. In a previous study, orientation of bare Mg was compared to that covered by MgO.[12] The significant experimental challenges in the isolation of specific grains for the collection of electrochemical single-grain data afforded an exact overlap between AFM morphology measurements of only two grain orientations (Figure 10). However, the systematic orientation-dependent variation in the surface morphology summarized in Figure 3 facilitates the discussion on the impact of crystallographic orientation and surface morphology on the electrochemical behavior, even without performing the experi-

ment on exactly the same grain orientations. All grains on Ni-11Cr which passivate are located in a region of the stereographic triangle which is expected to possess a surface similar to the matchstick morphology, while all grains which did not passivate are located in regions with aperiodic surface morphologies and often display high-aspect ratio asperities. This comparison demonstrates the significant influence of surface morphology at the nanoscale on the kinetics of oxidation. The atomic scale description of etching and passivation using the CN of a surface is inextricably linked with the mesoscale expression of surface morphologies.

An aperiodic surface likely favors a high nucleation density of oxides during passivation, but it is difficult to achieve a coherent and continuous surface coverage for the relatively high aspect ratio features. The asperities can locally enhance the internal Mott potential and external electric fields and contribute to failure of the passive layer. The nanofaceted surface can provide a similar breakdown mechanism at the edges of the crystallites, but the density of these "failure points" is significantly smaller, and they serve at the same time as primary nucleation sites for the oxide, as seen in the AFM images (Figure 10). The passive film might, therefore, be even thicker at the edges of the facets, minimizing this particular breakdown scenario and contributing to the overall stability of the passive layer.

Future work should examine the details discussed above as $(h\,k\,l)$ specificity alone is not sufficient to prescribe passivation tendency in its entirety. Specifically single-grain oxides, grain boundaries, and triple points should be included and investigated as a function of misorientation. The complexity of the passivation process which includes dissolution of alloy and oxide grains contributes to the difficulties in relating passivation to a single descriptor.

CONCLUSIONS

This work has presented, in detail, the orientation-dependence of electrochemically etched and passivated single grains on Ni-11Cr and Ni-11Cr-6Mo, wt %, in acidic chloride solutions. The oxide growth and passivation properties on Ni-11Cr conveyed using film growth kinetics, steady state film thicknesses, and associated electrochemical and passivation currents and express a strong dependence on the crystallographic orientation of each grain, but $\{h\,k\,l\}$ was insufficient specificity when etched. The global measurements, which average over many grains, are not sufficient to understand the passivation behavior of the alloy which occurs on a grain by grain basis. The presence of Mo mitigates the poor passivation behavior of some grains of near identical orientation in Ni-11Cr. In general, grains close to $(1\,0\,1)$ perform best in terms of passivation, which coincides with a refaceted surface of matchstick type morphology. This may have more to do with oxide epitaxy compared to surface energy. The systematic variation of nanoscale surface morphology within the crystallographic triangle can be understood by differential reactivity of the exposed terraces, connecting the atomic surface structure and average CN models used in previous work. In-operando analysis of the electrochemical passivation using single-frequency impedance enabled the measurement of i_{ox} independently from the significant dissolution. As such, accurate application of the Cabrera–Mott oxidation model was enabled, and fitting of kinetic parameters for Ni-11Cr-6Mo yielded experimental values for direct comparison with theoretical predictions. This work will be used for future development of the description of the passivation reaction for global and local measurements.

■ AUTHOR INFORMATION

Corresponding Author

*Phone: 434 924 7203. E-mail: pr6e@virginia.edu.

ORCID

Petra Reinke: 0000-0002-4544-5906

Notes

The authors declare no competing financial interest.

■ REFERENCES

(1) Fushimi, K.; Miyamoto, K.; Konno, H. Anisotropic Corrosion of Iron in PH 1 Sulphuric Acid. *Electrochim. Acta* **2010**, *55*, 7322−7327.

(2) Holme, B.; Ljones, N.; Bakken, A.; Lunder, O.; Lein, J. E.; Vines, L.; Hauge, T.; Bauger, O.; Nisancioglu, K. Preferential Grain Etching of AlMgSi(Zn) Model Alloys. *J. Electrochem. Soc.* **2010**, *157* (12), C424−C427.

(3) Hoseini, M.; Shahryari, A.; Omanovic, S.; Szpunar, J. A. Comparative Effect of Grain Size and Texture on the Corrosion Behaviour of Commercially Pure Titanium Processed by Equal Channel Angular Pressing. *Corros. Sci.* **2009**, *51* (12), 3064−3067.

(4) Krawiec, H.; Szklarz, Z. Combining the Electrochemical Microcell Technique and the Electron Backscatter Diffraction Method to Study the Electrochemical Behaviour of Polycrystalline Aluminium in Sodium Chloride Solution. *Electrochim. Acta* **2016**, *203*, 426−438.

(5) Liu, M.; Qiu, D.; Zhao, M. C.; Song, G.; Atrens, A. The Effect of Crystallographic Orientation on the Active Corrosion of Pure Magnesium. *Scr. Mater.* **2008**, *58* (5), 421−424.

(6) Martinez-Lombardia, E.; Gonzalez-Garcia, Y.; Lapeire, L.; De Graeve, I.; Verbeken, K.; Kestens, L.; Mol, J. M. C.; Terryn, H. Scanning Electrochemical Microscopy to Study the Effect of Crystallographic Orientation on the Electrochemical Activity of Pure Copper. *Electrochim. Acta* **2014**, *116*, 89−96.

(7) Schreiber, A.; Rosenkranz, C.; Lohrengel, M. M. Grain-Dependent Anodic Dissolution of Iron. *Electrochim. Acta* **2007**, *52*, 7738−7745.

(8) Song, J. M.; Zou, Y. S.; Kuo, C. C.; Lin, S. C. Orientation Dependence of the Electrochemical Corrosion Properties of Electrodeposited Cu Foils. *Corros. Sci.* **2013**, *74* (9), 223−231.

(9) Rhodin, T. N. Low Temperature Oxidation of Copper. I. Physical Mechanism. *J. Am. Chem. Soc.* **1950**, *72*, 5102−5106.

(10) Yang, J. C.; Kolasa, B.; Gibson, J. M.; Yeadon, M. Self-Limiting Oxidation of Copper. *Appl. Phys. Lett.* **1998**, *73* (19), 2841−2843.

(11) Young, F. W.; Cathcart, J. V.; Gwathmey, A. T. The Rates of Oxidation of Several Faces of a Single Crystal of Copper as Determined with Elliptically Polarized Light. *Acta Metall.* **1956**, *4* (2), 145−152.

(12) Bland, L. G.; Gusieva, K.; Scully, J. R. Effect of Crystallographic Orientation on the Corrosion of Magnesium: Comparison of Film Forming and Bare Crystal Facets Using Electrochemical Impedance and Raman Spectroscopy. *Electrochim. Acta* **2017**, *227*, 136−151.

(13) Koroleva, E. V.; Thompson, G. E.; Skeldon, P.; Noble, B. Crystallographic Dissolution of High Purity Aluminium. *Proc. R. Soc. London, Ser. A* **2007**, *463* (2083), 1729−1748.

(14) Lillard, R. S. Factors Influencing the Transition from Metastable to Stable Pitting in Single-Crystal Beryllium. *J. Electrochem. Soc.* **2001**, *148* (1), B1−B11.

(15) Davis, B. W.; Moran, P. J.; Natishan, P. M. Metastable Pitting Behavior of Aluminum Single Crystals. *Corros. Sci.* **2000**, *42* (12), 2187−2192.

(16) Schreiber, A.; Schultze, J. W.; Lohrengel, M. M.; Kármán, F.; Kálmán, E. Grain Dependent Electrochemical Investigations on Pure Iron in Acetate Buffer PH 6.0. *Electrochim. Acta* **2006**, *51*, 2625−2630.

(17) Shahryari, A.; Szpunar, J. A.; Omanovic, S. The Influence of Crystallographic Orientation Distribution on 316LVM Stainless Steel Pitting Behavior. *Corros. Sci.* **2009**, *51* (3), 677−682.

(18) Yasuda, M.; Weinberg, F.; Tromans, D. Pitting Corrosion of Al and Al-Cu Single Crystals. *J. Electrochem. Soc.* **1990**, *137* (12), 3708−3715.

(19) Konig, U.; Davepon, B. Microstructure of Polycrystalline Ti and Its Microelectrochemical Properties by Means of Electron-Backscattering Diffraction (EBSD). *Electrochim. Acta* **2001**, *47*, 149−160.

(20) Fushimi, K.; Kurauchi, K.; Yamamoto, Y.; Nakanishi, T.; Hasegawa, Y.; Ohtsuka, T. Growth and Degradation of an Anodic Oxide Film on Titanium in Sulphuric Acid Observed by Ellipso-Microscopy. *Electrochim. Acta* **2014**, *144*, 56−63.

(21) Takabatake, Y.; Kitagawa, Y.; Nakanishi, T.; Hasegawa, Y.; Fushimi, K. Grain Dependency of a Passive Film Formed on Polycrystalline Iron in PH 8.4 Borate Solution. *J. Electrochem. Soc.* **2017**, *164* (7), C349−C355.

(22) Horton, D. J.; Zhu, A. W.; Scully, J. R.; Neurock, M. Crystallographic Controlled Dissolution and Surface Faceting in Disordered Face-Centered Cubic FePd. *MRS Commun.* **2014**, *4* (03), 113−119.

(23) Kao, K. C. Theory of High-Field Electric Conduction and Breakdown in Dielectric Liquids. *IEEE Trans. Electr. Insul.* **1976**, *EI-11* (4), 121−128.

(24) Zhang, W. B.; Chen, C.; Zhang, S. Y. Equilibrium Crystal Shape of Ni from First Principles. *J. Phys. Chem. C* **2013**, *117* (41), 21274−21280.

(25) Barsotti, T.; Bermond, J. M.; Drechsler, M. A Measurement of the Surface Energy Anisotropy of Nickel by Transmission Electron Microscopy of Field Emitter Crystals. *Surf. Sci.* **1984**, *146* (2−3), 467−479.

(26) Vitos, L.; Ruban, A. V.; Skriver, H. L.; Kollár, J. The Surface Energy of Metals. *Surf. Sci.* **1998**, *411* (1−2), 186−202.

(27) Marks, L. Competitive Chloride Chemisorption Disrupts Hydrogen Bonding Networks: DFT, Crystallography, Thermodynamics and Morphological Consequences. *Corrosion* **2018**, *74* (3), 295−311.

(28) Tokuda, T.; Ives, M. B. Pitting Corrosion of Ni. *Corros. Sci.* **1971**, *11* (5), 297−306.

(29) Latanision, R. M.; Opperhauser, H. Passivation of Nickel Monocrystal Surfaces. *Corrosion* **1971**, *27* (12), 509−515.

(30) Machet, A.; Galtayries, A.; Zanna, S.; Klein, L.; Maurice, V.; Jolivet, P.; Foucault, M.; Combrade, P.; Scott, P.; Marcus, P. XPS and STM Study of the Growth and Structure of Passive Films in High Temperature Water on a Nickel-Base Alloy. *Electrochim. Acta* **2004**, *49*, 3957−3964.

(31) Gwathmey, A. T.; Lawless, K. R. *The Surface Chemistry of Metals and Semiconductors*; John Willy & Sons, Inc.: New York, 1960.

(32) Luo, L.; Zou, L.; Schreiber, D. K.; Olszta, M. J.; Baer, D. R.; Bruemmer, S. M.; Zhou, G.; Wang, C.-M. In Situ Atomic Scale Visualization of Surface Kinetics Driven Dynamics of Oxide Growth on a Ni−Cr Surface. *Chem. Commun.* **2016**, *52* (16), 3300−3303.

(33) Luo, L.; Zou, L.; Schreiber, D. K.; Baer, D. R.; Bruemmer, S. M.; Zhou, G.; Wang, C. M. In-Situ Transmission Electron Microscopy Study of Surface Oxidation for Ni-10Cr and Ni-20Cr Alloys. *Scr. Mater.* **2016**, *114*, 129−132.

(34) Gray, J. J.; El Dasher, B. S.; Orme, C. A. Competitive Effects of Metal Dissolution and Passivation Modulated by Surface Structure: An AFM and EBSD Study of the Corrosion of Alloy 22. *Surf. Sci.* **2006**, *600* (12), 2488−2494.

(35) Ebrahimi, N.; Jakupi, P.; Korinek, A.; Barker, I.; Moser, D. E.; Shoesmith, D. W. Sigma and Random Grain Boundaries and Their Effect on the Corrosion of the Ni-Cr-Mo Alloy 22. *J. Electrochem. Soc.* **2016**, *163* (5), C232−C239.

(36) Hirth, J. P.; Pieraggi, B.; Rapp, R. A. The Role of Interface Dislocations and Ledges as Sources/Sinks for Point Defects in Scaling Reactions. *Acta Metall. Mater.* **1995**, *43* (3), 1065−1073.

(37) Chao, C. Y.; Lin, L. F.; Macdonald, D. D. A Point Defect Model for Anodic Passive Films I. Film Growth Kinetics. *J. Electrochem. Soc.* **1981**, *128* (6), 1187−1194.

(38) Fehlner, F. P.; Mott, N. F. Low-Temperature Oxidation. *Oxid. Met.* **1970**, *2* (1), 59−99.

(39) Seyeux, A.; Maurice, V.; Marcus, P. Oxide Film Growth Kinetics on Metals and Alloys: I. Physical Model. *J. Electrochem. Soc.* **2013**, *160* (6), C189−C196.

(40) Beverskog, B.; Bojinov, M.; Kinnunen, P.; Laitinen, T.; Mäkelä, K.; Saario, T. A Mixed-Conduction Model for Oxide Films on Fe, Cr and Fe-Cr Alloys in High-Temperature Aqueous Electrolytes - II. Adaptation and Justification of the Model. *Corros. Sci.* **2002**, *44* (9), 1923−1940.

(41) Cabrera, N.; Mott, N. F. Theory of the Oxidation of Metals. *Rep. Prog. Phys.* **1949**, *12* (1), 163−184.

(42) O'Dwyer, J. J. Theory of High Field Conduction in a Dielectric. *J. Appl. Phys.* **1969**, *40* (10), 3887−3890.

(43) Davenport, A. J.; Lee, B. K. Passive Film Growth Kinetics for Iron and Stainless Steel. *Electrochem. Soc. Proceed.* **2002**, 187−197.

(44) Macdonald, D. D. The Point Defect Model for the Passive State. *J. Electrochem. Soc.* **1992**, *139* (12), 3434−3449.

(45) Engler, O.; Randle, V. *Introduction to Texture Analysis: Macrotexture, Microtexture, and Orientation Mapping*; CRC Press: Boca Raton, FL, 2010.

(46) Policastro, S. A.; Auyeung, R. C. Y.; Martin, F. J.; Rayne, R. J.; Pique, A.; Lewis, A.; Geltmacher, A.; Natishan, P. M. An Approach for Determining Microscale Electrochemical Behavior. *J. Electrochem. Soc.* **2012**, *159* (1), C15−C24.

(47) Nečas, D.; Klapetek, P. Gwyddion: An Open-Source Software for SPM Data Analysis. *Cent. Eur. J. Phys.* **2012**, *10* (1), 181−188.

(48) Lutton, K.; Gusieva, K.; Ott, N.; Birbilis, N.; Scully, J. R. Understanding Multi-Element Alloy Passivation in Acidic Solutions Using Operando Methods. *Electrochem. Commun.* **2017**, *80* (7), 44−47.

(49) Hirschorn, B.; Orazem, M. E.; Tribollet, B.; Vivier, V.; Frateur, I.; Musiani, M. Constant-Phase-Element Behavior Caused by Resistivity Distributions in Films: I. Theory. *J. Electrochem. Soc.* **2010**, *157* (12), C452−C457.

(50) Macdonald, D. D.; Sun, A.; Priyantha, N.; Jayaweera, P. An Electrochemical Impedance Study of Alloy-22 in NaCl Brine at Elevated Temperature: II. Reaction Mechanism Analysis. *J. Electroanal. Chem.* **2004**, *572* (2), 421−431.

(51) Xu, Z.; Rosso, K. M.; Bruemmer, S. Metal Oxidation Kinetics and the Transition from Thin to Thick Films. *Phys. Chem. Chem. Phys.* **2012**, *14* (42), 14534−14539.

(52) Burstein, G. T.; Davenport, A. J. The Current-Time Relationship during Anodic Oxide Film Growth under High Electric Field. *J. Electrochem. Soc.* **1989**, *136* (4), 936−941.

(53) Braunbek, W. Eine Gittertheoretische Berechnung Der Elektrolytischen Leitfähigkeit Des Steinsalzkristalls. *Arch. Elektrotech.* **1927**, *19* (1), 115−122.

(54) Güntherschulze, A.; Betz, H. Die Bewegung Der Ionengitter von Isolatoren Bei Extremen Elektrischen Feldstärken. *Eur. Phys. J. A* **1934**, *92* (5), 367−374.

(55) Verwey, E. J. Electrolytic Conduction of a Solid Insulator at High Fields: The Formation of the Anodic Oxide Film on Aluminium. *Physica* **1935**, *2* (1−12), 1059−1063.

(56) Jakupi, P.; Zagidulin, D.; Noël, J. J.; Shoesmith, D. W. The Impedance Properties of the Oxide Film on the Ni-Cr-Mo Alloy-22 in Neutral Concentrated Sodium Chloride Solution. *Electrochim. Acta* **2011**, *56*, 6251−6259.

(57) Hayes, J. R.; Gray, J. J.; Szmodis, A. W.; Orme, C. A. Influence of Chromium and Molybdenum on the Corrosion of Nickel-Based Alloys. *Corrosion* **2006**, *62* (6), 491−500.

(58) Bocher, F.; Huang, R.; Scully, J. R. Prediction of Critical Crevice Potentials for Ni-Cr-Mo Alloys in Simulated Crevice Solutions as a Function of Molybdenum Content. *Corrosion* **2010**, *66* (5), 1−15.

(59) Lloyd, A. C.; Noël, J. J.; McIntyre, N. S.; Shoesmith, D. W. The Open-Circuit Ennoblement of Alloy C-22 and Other Ni-Cr-Mo Alloys. *JOM* **2005**, *57* (1), 31−35.

(60) Maurice, V.; Peng, H.; Klein, L. H.; Seyeux, A.; Zanna, S.; Marcus, P. Effects of Molybdenum on the Composition and Nanoscale Morphology of Passivated Austenitic Stainless Steel Surfaces. *Faraday Discuss.* **2015**, *180*, 151−170.

(61) Lloyd, A. C.; Noël, J. J.; McIntyre, S.; Shoesmith, D. W. Cr, Mo and W AClloying Additions in Ni and Their Effect on Passivity. *Electrochim. Acta* **2004**, *49*, 3015−3027.

(62) Pourbaix, M. *Atlas of Electrochemical Equilibria in Aqueous Solutions*; National Association of Corrosion Engineers, 1974.

(63) Wu, B.; Scully, J. R.; Hudson, J. L.; Mikhailov, A. S. Cooperative Stochastic Behavior in Localized Corrosion I. Model. *J. Electrochem. Soc.* **1997**, *144* (5), 1614−1620.

(64) Shibata, T.; Takeyama, T. Stochastic Theory of Pitting Corrosion. *Corrosion* **1977**, *33* (7), 243−251.

(65) Frankel, G. S.; Stockert, L.; Hunkeler, F.; Boehni, H. Metastable Pitting of Stainless Steel. *Corrosion* **1987**, *43* (7), 429−436.

(66) Marikar, P.; Brodsky, M. B.; Sowers, C. H.; Zaluzec, N. J. In-Situ HVEM Studies of the Early Stages of Oxidation of Nickel and Nickel-Chromium Alloys. *Ultramicroscopy* **1989**, *29* (1−4), 247−256.

(67) Yang, J. C.; Yeadon, M.; Kolasa, B.; Gibson, J. M. Oxygen Surface Diffusion in Three-Dimensional Cu_2O Growth on Cu(001) Thin Films. *Appl. Phys. Lett.* **1997**, *70* (26), 3522−3524.

(68) Mrowec, S.; Grzesik, Z. Oxidation of Nickel and Transport Properties of Nickel Oxide. *J. Phys. Chem. Solids* **2004**, *65* (10), 1651−1657.

(69) McCafferty, E. Graph Theory and the Passivity of Binary Alloys. *Corros. Sci.* **2000**, *42* (11), 1993−2011.

(70) McCafferty, E. Oxide Networks, Graph Theory, and the Passivity of Binary Alloys. *Corros. Sci.* **2002**, *44* (7), 1393−1409.

(71) McCafferty, E. Relationship Between Graph Theory and Percolation Approaches in the Passivity of Fe−Cr Binary Alloys. *J. Electrochem. Soc.* **2008**, *155* (10), C501−C505.

(72) McCafferty, E. *Introduction to Corrosion Science*; Springer: New York, 2010.

(73) Scully, J. R. Corrosion Chemistry Closing Comments: Opportunities in Corrosion Science Facilitated by Operando Experimental Characterization Combined with Multi- Scale Computational Modelling. *Faraday Discuss. Faraday Discuss.* **2015**, *180* (180), 577−593.

(74) Sugimoto, K.; Sawada, Y. Role of Alloyed Molybdenum in Austenitic Stainless Steels in the Inhibition of Pitting in Neutral Halide Solutions. *Corrosion* **1976**, *32* (9), 347−352.

(75) Kobe, B.; Badley, M.; Henderson, J. D.; Anderson, S.; Biesinger, M. C.; Shoesmith, D. Application of Quantitative X-Ray Photoelectron Spectroscopy (XPS) Imaging: Investigation of Ni-Cr-Mo Alloys Exposed to Crevice Corrosion Solution. *Surf. Interface Anal.* **2017**, *49* (13), 1345−1350.

(76) Olefjord, I.; Elfstrom, B.-O. The Composition of the Surface during Passivation of Stainless Steels. *Corrosion* **1982**, *38* (1), 46−52.

(77) Sugimoto, K.; Sawada, Y. The Role of Molybdenum Additions to Austenitic Stainless Steels in the Inhibition of Pitting in Acid Chloride Solutions. *Corros. Sci.* **1977**, *17* (5), 425−445.

(78) Willenbruch, R. D.; Clayton, C. R.; Oversluizen, M.; Kim, D.; Lu, Y. An XPS and Electrochemical Study of the Influence of Molybdenum and Nitrogen on the Passivity of Austenitic Stainless Steel. *Corros. Sci.* **1990**, *31* (C), 179−190.

(79) Bojinov, M.; Fabricius, G.; Laitinen, T.; Mäkelä, K.; Saario, T.; Sundholm, G. Influence of Molybdenum on the Conduction Mechanism in Passive Films on Iron-Chromium Alloys in Sulphuric Acid Solution. *Electrochim. Acta* **2001**, *46*, 1339−1358.

(80) Yang, W.; Ni, R. C.; Hua, H. Z.; Pourbaix, A. The Behavior of Chromium and Molybdenum in the Propagation Process of Localized Corrosion of Steels. *Corros. Sci.* **1984**, *24* (8), 691−707.

(81) De Vito, E.; Marcus, P. XPS Study of Passive Films Formed on Molybdenum-Implanted Austenitic Stainless Steel. *Surf. Interface Anal.* **1992**, *19* (1−12), 403−408.

(82) Yun, D. W.; Seo, H. S.; Jun, J. H.; Lee, J. M.; Kim, K. Y. Molybdenum Effect on Oxidation Resistance and Electric Conduction of Ferritic Stainless Steel for SOFC Interconnect. *Int. J. Hydrogen Energy* **2012**, *37* (13), 10328−10336.

(83) Olefjord, I. The Passive State of Stainless Steels. *Mater. Sci. Eng.* **1980**, *42* (C), 161−171.

(84) Kim, D.; Kagwade, S. V.; Clayton, C. R. Identification of Mo (V) Commonly Observed in Passive Films Formed on Stainless Steels. *Surf. Interface Anal.* **1998**, *26* (9), 155−159.

(85) Mishra, A. K.; Shoesmith, D. W. The Activation/Depassivation of Nickel-Chromium-Molybdenum Alloys: An Oxyanion or a PH Effect - Part II. *Electrochim. Acta* **2013**, *102*, 328−335.

(86) Mishra, A. K.; Ramamurthy, S.; Biesinger, M.; Shoesmith, D. W. The Activation/Depassivation of Nickel-Chromium-Molybdenum Alloys in Bicarbonate Solution: Part I. *Electrochim. Acta* **2013**, *100*, 118−124.

(87) Ebrahimi, N.; Biesinger, M. C.; Shoesmith, D. W.; Noël, J. J. The Influence of Chromium and Molybdenum on the Repassivation of Nickel-Chromium-Molybdenum Alloys in Saline Solutions. *Surf. Interface Anal.* **2017**, *49* (13), 1359−1363.

(88) Zhang, X.; Zagidulin, D.; Shoesmith, D. W. Characterization of Film Properties on the NiCrMo Alloy C-2000. *Electrochim. Acta* **2013**, *89*, 814−822.

(89) Urquidi, M.; Macdonald, D. D. Solute-Vacancy Interaction Model and the Effect of Minor Alloying Elements on the Initiation of Pitting Corrosion. *J. Electrochem. Soc.* **1985**, *132* (3), 555−558.

(90) Urquidi-Macdonald, M.; Macdonald, D. D. Theoretical Analysis of the Effects of Alloying Elements on Distribution Functions of Passivity Breakdown. *J. Electrochem. Soc.* **1989**, *136* (4), 961−967.

(91) Samin, A. J.; Taylor, C. D. First-Principles Investigation of Surface Properties and Adsorption of Oxygen on Ni-22Cr and the Role of Molybdenum. *Corros. Sci.* **2018**, *134*, 103−111.

(92) Gray, J. J.; Hayes, J. R.; Gdowski, G. E.; Viani, B. E.; Orme, C. A. Influence of Solution PH, Anion Concentration, and Temperature on the Corrosion Properties of Alloy 22. *J. Electrochem. Soc.* **2006**, *153* (3), B61−B67.

(93) Masel, R. I. *Principles of Adsorption and Reaction on Solid Surfaces*; Wiley: New York, 1996.